Characterization of Ca-phosphate biological materials by scanning transmission x-ray microscopy (STXM) at the Ca L 2,3 -, P L 2,3 -and C K- edges

Julie Cosmidis, Karim Benzerara, Nadine Nassif, Tolek Tyliszczak, Franck Bourdelle

Characterization of Ca-phosphate biological materials by scanning transmission x-ray microscopy (STXM) at the Ca $L_{2,3}$-, P $L_{2,3}$- and C K-edges

Julie Cosmidis[a], Karim Benzerara[a], Nadine Nassif[b], Tolek Tyliszczak[c], Franck Bourdelle[d]

a. Institut de Minéralogie, de Physique des Matériaux, et de Cosmochimie (IMPMC), Sorbonne Universités, Univ Paris 06, CNRS UMR 7590, MNHN, IRD UMR 206, F-75252 Paris 05, France
b. Lab Chim Matière Condensée (LMCM), Univ Paris 06, Coll France, CNRS UMR 7574, F-75231 Paris 05, France
c. Lawrence Berkeley National Laboratory, Advanced Light Source, Berkeley, CA 94720 USA
d. GeoRessources Laboratory, Université de Lorraine, UMR CNRS 7359, F-54506 Vandoeuvre Les Nancy, France

Corresponding author :

Karim Benzerara, Institut de Minéralogie, de Physique des Matériaux et de Cosmochimie, 4 place Jussieu, 75252 Paris cedex 05, France.

Email : karim.benzerara@impmc.upmc.fr. Phone : *+33 1 44 27 75 42*

Abstract

Several naturally-occurring biological materials, including bones and teeth, pathological calcifications, microbial mineral deposits formed in marine phosphogenesis areas, as well as bio-inspired cements used for bone and tooth repair, are composed of Ca-phosphates. These materials are usually identified and characterized using bulk-scale analytical tools such as XRD, FTIR or NMR. However, there is a need for imaging techniques that provide information on the spatial distribution and chemical composition of the Ca-phosphate phases at the micrometer-scale and nanometer-scale. Indeed, such analyses provide insightful indications on how the materials may have formed, *e.g.,* through transient precursor phases that eventually remain spatially separated from the mature phase. Here, we present STXM analyses of Ca-phosphate reference compounds, showing the feasibility of fingerprinting Ca-phosphate-based materials. We calibrate methods to determine important parameters of Ca-phosphate phases such as their Ca/P ratio and carbonate content at the ~25 nm scale using XANES spectra at the C K-, Ca $L_{2,3}$- and P $L_{2,3}$-edges. As an illustrative case study, we also perform STXM analyses on hydroxyapatite precipitates formed in a dense fibrillar collagen matrix. This study paves the way for future research on Ca-phosphate biomineralization processes down to the scale of a few tens of nanometers.

1 Introduction

A diversity of Ca-phosphate-based materials occur naturally, differing by their chemical composition and mineralogical structure (Table 1). The major mineral phase composing bones and teeth of vertebrates is carbonate-hydroxyapatite (CHA) [1–3]. CHA can also be found in pathological calcification occurring in various parts of the body, including kidneys, cardiac valves and teeth, together with octacalcium phosphate, brushite or whitlockite [1,4]. Marine phosphorites, presumably formed by microbial activity, are mostly composed of carbonate-fluoroapatite (CFA) [5,6]. Ca-polyphosphates, forming in eukaryotic and prokaryotic cells [7,8], are thought to play an important role in the formation of sedimentary CFA [9,10] and it has also been proposed that they could play a role in apatite biomineralization in bones [11]. Finally, brushite, monetite and tricalcium phosphate often compose biomimetic cements used for the repair of damaged bones and teeth [12,13].

The different Ca-phosphates and polyphosphates partly differ by their Ca/P ratios (Table 1). Ca/P ratios can therefore be used as a fingerprint of these phases. However, there can be significant variations of the Ca/P ratio for a given phase. For example, the apatitic mineral phase composing vertebrate bones is sometimes referred to as Ca-deficient hydroxyapatite (CDHA), with a Ca/P ratio ~1.5, compared to 1.67 for stoichiometric HA. Such a variation has great importance since the chemical and biological properties of CDHA are strongly dependent on their Ca/P ratios. For instance, the decrease of the Ca/P ratio is associated with increase of structural disorder ([14] and references therein), which could explain the higher solubility [15] and degradation rate in solution [16] of CDHA compared to stoichiometric HA.

The carbonate content is another important parameter influencing Ca-phosphate properties. CHA in bones and teeth or CFA in sediments contain carbonate ions (CO_3^{2-}) which

may be located in the *c*-axis anion channels of apatite (A-site) or substitute for tetrahedral PO_4^{3-} groups (B-site) [17]. Incorporation of CO_3^{2-} has important effects on the physical and chemical properties of apatite [3]. For example, the solubility product of CHA in enamel is several orders of magnitudes greater than that of stoichiometric HA [1,18]. The presence of CO_3^{2-} also increases the dissolution rate of apatite in acids [19,20]. CO_3^{2-} substitution in apatite is generally associated with a decreased crystallinity [21–23], which results in altered mechanical properties (modulus and hardness) [24].

Characterization of Ca-phosphate biological materials (*e.g.,* phase identification, Ca/P ratio, CO_3^{2-} content…) is usually achieved using bulk methods such as x-ray diffraction (XRD) (*e.g.*, [25,26]), Fourier-Transform infrared (FTIR) spectroscopy (*e.g.*, [27,28]), Raman spectroscopy (e.g., [29,30]), or nuclear magnetic resonance (NMR) (*e.g.*, [31,32]). However, there is also a need for imaging techniques that provide information on the submicrometer-scale spatial distribution and chemical composition of the Ca-phosphate phases, as well as on the way they are associated with the organic matrix within which they formed. Such spatial information may indeed provide insightful indications on how these materials formed. For instance, it has been suggested that the formation of bones proceeds through the replacement of transient non-apatitic mineral phases such as amorphous Ca-phosphate [33,34] or octacalcium phosphate [29,35]. However, the newly forming bone mineral might alternatively be composed of nano-sized and poorly crystalline apatite with non-apatitic minerals at its surface [36]. This question of the existence and nature of the precursor phase(s) of bone minerals is still debated [2]. Transient precursor phases of Ca-phosphate biominerals might sometimes be physically separated from mature phases, but they very often occur as fine mixtures with them (*e.g.*, [25]). Discriminating and characterizing different Ca-phosphate phases at the few nanometer-scale would be of great interest for gaining further insights into these issues.

Transmission electron microscopy (TEM) which allows for high resolution imaging, electron diffraction, energy-dispersive x-ray spectroscopy (EDXS) and electron energy loss spectroscopy (EELS) to be performed has often been employed to study the initial stages of tissue mineralization (*e.g.,* [37–42]). For example, single-crystal electron diffraction patterns have been used to characterize mixtures of several Ca-phosphates including TCP, OCP and HA [38,39,41], but as pointed out by Leng et al. [38], electron diffraction ring patterns can be controversial and used for Ca-phosphates identification only very cautiously. Moreover, irradiation by the electron beam can induce damages in the precursor phases as well as alter their spatial relations with the organic matrix [35]. For instance, Ca/P ratios of synthetic hydroxyapatites have shown to be modified by beam-induce damages that occur during TEM-EDXS and EELS analyses [43]. Finally, TEM usually provides only limited information on the chemical composition of the organic matrix.

Synchrotron-based scanning transmission (soft) x-ray microscopy (STXM) is a microscopy technique providing chemical speciation-sensitive images at a spatial resolution down to ~25 nm coupled with x-ray absorption near edge spectra (XANES) over a relatively extended range of energies (between 100 and 2000 eV). It allows characterizing the speciation (*i.e.*, coordination and/or redox state) of various elements including the major elements of Ca-phosphates (*e.g.*, Ca and P) as well as associated carbonate ions and organic molecules. Moreover, STXM induces relatively lower beam damages compared to TEM-based techniques [44,45]. A number of studies on biomineral formation, including hydroxyapatite biomineralization (see [46] and references therein) have used STXM/XANES spectromicroscopy previously, but they did not use information provided by this technique to its full extent.

Several studies characterizing reference Ca-phosphates by bulk–scale XANES spectroscopy at the Ca $L_{2,3}$-edges [33,47,48] and P $L_{2,3}$-edges [49,50] have been published in

the past. The present study includes XANES spectra at the P and Ca $L_{2,3}$-edges and the C K-edge acquired by STXM for a large number of reference Ca-phosphates and polyphosphates. It provides qualitative and quantitative approaches for the characterization of Ca-phosphate-based materials at the ~25 nm-scale, including (i) fingerprinting of these phases, notably using Ca/P ratios, and (ii) estimation of the carbonate content of apatites.

2 Materials and Methods

2.1 Reference compounds

The reference compounds analyzed in this study are marked by an asterisk in Table 1, where abbreviations and generic formula are also given.

Some of the Ca-phosphate and polyphosphate reference compounds were purchased from Sigma-Aldrich Co.: hydroxyapatite nanopowder (HA), α-tricalcium phosphate (α-TCP), amorphous calcium phosphate (ACP), and sodium polyphosphate ($Na_{(n+2)}P_nO_{(3n+1)}$, n = 45±5) (Na-PP). The composition and purity of these samples was checked by XRD using a Bruker D2 Phaser XRD desktop system with a Cu-kα radiation, except for the Na-PP which is sold by Sigma-Aldrich as a glass (sodium phosphate glass) (Supplementary Information, Fig. S1). Other reference compounds were synthesized and provided by Frédérique Pourpoint: dicalcium phosphate dihydrate (mineral brushite, DCPD), monocalcium phosphate monohydrate (MCPM), β-tricalcium phosphate (β-TCP) and tetracalcium phosphate (TTCP), Ca-polyphosphate (β-$Ca(PO_3)_2$) (PP), and dicalcium phosphate anhydrous (mineral monetite, DCPA). These samples were synthesized and characterized by bulk methods previously and the results of these characterizations were published in [51]-[53]. Two synthetic biomimetic carbonated hydroxyapatites (CHA1, CHA 2), referred as HA-1 and HA-2 in [54] and differing by their carbonate concentrations, were also used. They were characterized by XRD, NMR, and FTIR as detailed in [54]. Their carbonate concentrations were measured by

thermogravimetric analysis and are respectively ~2.2 and ~4.9 wt% CO_3^{2-} (Stanislas Von Euw, Personal communication).

Other reference compounds were natural samples from the field. The carbonate fluoroapatite (mineral francolite, CFA) sample was collected in the sedimentary phosphate deposit of Ouled Abdoun (Morocco) and characterized by bulk XRD measurements [55]. Its carbonate content was ~6.9 wt% CO_3^{2-} as shown by the empirical relation between the carbonate content of CFA and the $\Delta(2\theta)$ difference between the (004) and (410) XRD peaks derived from Schuffert et al. [56]. It contained 37.9 wt% Ca, 14.5 wt% P and 4.2 wt% F as assessed by electron microprobe analyses. A tooth from a Camelidae (T1 in [57]) and a bone from an unidentified animal (probably a donkey) [58] from the Tugen Hills (Great Rift Valley, Kenya) were also used and characterized by bulk FTIR [57,58]. Their elemental compositions, determined by atomic absorption spectroscopy, were 35 wt% Ca, 17.8 wt% P and 80 ppm F for the tooth sample, and 24.7 wt% Ca, 13.21 wt% P, and 1622 ppm F for the bone sample (Haohao Yi, personal communication).

Finally, a bone-like matrix (Coll/CHA/SBF in [40]) obtained by co-precipitation of calcium-phosphate salts and collagen molecules in a simulated body fluid was studied.

2.2 Sample preparation for STXM

All reference samples except the Coll/CHA/SBF matrix were gently ground in pure ethanol in an agate mortar. About 2 µL of each sample were deposited on Si_3Ni_4 windows. The samples were then dried at ambient temperature.

The Coll/CHA/SBF matrix was fixed with glutaraldehyde, washed in a cacodylate/saccharose buffer solution, dehydrated and embedded in araldite. A thin section (80 nm) deposited on a TEM grid was used for STXM analyses.

2.3 Data acquisition and spectral processing

STXM/XANES analyses were performed on beamline 11.0.2.2 at the Advanced Light Source (Lawrence Berkeley National Laboratory, Berkeley, USA) [59] and the SM beamline at the Canadian Light Source (Saskatoon, Canada) [60]. Methods for STXM analyses and data processing can be found, for example, in Bourdelle et al. [61] and Cosmidis and Benzerara [46]. For each compound, stacks at the Ca $L_{2,3}$-edges (340-370 eV) and sometimes the P $L_{2,3}$-edges (125-190 eV) or the C K edge (260-320 eV) were acquired on an area containing one or several particles. When multiples stacks were acquired at the same area different edges, they had the same pixel number and size, so that they could be appended in a single stack. XANES spectra were then extracted from these stacks using aXis2000 [62]. Energy calibration at the C K-edge was performed using the 3p Rydberg peak at 294.96 eV of gaseous CO_2 flushed into the STXM chamber. The energy position of the major peak on the L_2 edge of Ca was set to 352.5 eV for all reference spectra. For spectra at the P $L_{2,3}$-edges on Fig. 2, the energy of the first peak was set to 136.7 eV.

Absorption saturation effects, caused by sample thickness, are frequent at the Ca $L_{2,3}$-edges, and cause distortions of the XANES spectra [63]. In order to avoid such spectral distortions, the spectra of the reference Ca-phosphate compounds were extracted from areas showing a maximum optical density (OD) value <1 at 349.2 eV (energy of the major peak on the Ca L_3 edge) (see Supplementary Information, Fig. S2).

A linear background correction was applied to the spectra at the Ca $L_{2,3}$-, P $L_{2,3}$-, and C K-edges by setting the baseline in the 340-345 eV, 125-134 eV and 260-280 eV regions, respectively, to an horizontal line at 0, in order to eliminate the contribution of lower energy absorption. The edge steps at the Ca $L_{2,3}$-edges and P $L_{2,3}$-edges resulting from transitions to the continuum were subtracted using double arctan functions, as described in [61]. These two

operations (linear background correction and double arctan subtraction), applied to the Ca $L_{2,3}$-edge spectrum of HA, are illustrated in Fig. S3.

3 Results

3.1 XANES spectroscopy of Ca-phosphate reference compounds at the Ca and P $L_{2,3}$-edges

3.1.1 XANES analyses at the Ca $L_{2,3}$-edges of Ca-phosphates reference compounds

Ca $L_{2,3}$-edge XANES spectra were measured for 9 Ca-phosphate reference compounds (Fig. 1). The energy positions of the peaks in these spectra are given in Table 2.

The positions of the main L_2 peak (~352.5 eV) and L_3 peak (~349.2 eV) are very similar for all analyzed compounds. However, variations exist in the positions and relative intensities of smaller pre-edge peaks (thereafter called a_3-d_3 and a_2-c_2) among the different Ca-phosphates. In most XANES spectra (TTCP, HA, α-TCP, DCPA, DCPD, MCPM), there are two small peaks (or a small peak and a shoulder) a_3 and b_3, of about the same intensity, with a third more intense peak c_3. This pattern is characteristic of an octahedral crystal field [48]. Alpha- and β-TCP are two polymorphs of $Ca_3(PO_4)_2$, α-TCP being the high-temperature form and β-TCP the low temperature one. The structure of α-TCP is related to that of HA [64] which is reflected by very similar Ca $L_{2,3}$-edges XANES spectra for α-TCP and HA. In contrast, β-TCP has a very distinct spectrum, consistently with a different local electronic environment of Ca in this polymorph [65]. Ca-polyphosphate (also called Ca metaphosphate) β-$Ca(PO_3)_2$ (PP) exhibits long polymeric chains of PO_4^{3-} arranged in a zigzag configuration where Ca^{2+} are intercalated as charge-balancing ions, sharing only partially covalent bonds with O atoms [52, 66].

3.1.2 XANES analyses at the P L_{2-3}-edges of Ca-phosphate reference compounds

Most previous XANES studies of P minerals have focused on the P K-edge at ~2150 eV [67–71]. Soft x-ray STXM allows for the measurement of XANES spectra at the P $L_{2,3}$-edges which lie at around 130-150 eV. XANES spectroscopy at the P $L_{2,3}$-edges is technically more difficult to perform because of high absorption at these low energies but it provides much information on P speciation [50], and therefore may allow a very good identification of crystalline and amorphous P-bearing minerals, which owing to the use of STXM can be conducted at the submicrometer-scale.

Figure 2 shows XANES spectra at the P $L_{2,3}$-edges of several reference Ca-phosphate compounds. The two peaks a (at ~136.7 eV) and b (at ~137.6 eV) correspond to the L_3 and L_2 edges, respectively. The ~1 eV energy separation between these two peaks is insensitive to the chemical environment of P [50], and is therefore the same for all compounds. At higher energies, a broad peak (c) is observed for Na-PP and MCPM, whereas two peaks (c and d, at ~138.4 and ~139.0 eV, respectively) can be distinguished for the other compounds (DCPA, α-TCP and HA). The positions of peaks a, b, c and d are similar for all compounds (except for peak d in the spectrum of DCPA which is slightly shifted towards higher energies at ~139.3 eV). However, the relative intensities of these peaks vary among the different compounds spectra. The shoulder at ~142 eV (peak e) is a common characteristic of all Ca-phosphates [50], and has been interpreted as the result of transitions from P 2p to empty Ca 3d orbitals. It is however present (but much fainter) in the Na-PP spectrum (which does not contain Ca). The broad peak at ~146.9 eV (peak f) is sometimes called the “shape resonance”, and its position is sensitive to the local chemical environment of P. It appears to be split into two broad peaks in the Na-PP spectrum. The spectrum of Na-PP presented here is similar to

previously published spectra of calcium-pyrophosphate (CPP) [49,50], indicating that the local chemical environment of P is similar in both compounds.

3.1.3 Assessment of Ca/P ratios in Ca-phosphates using STXM at the Ca $L_{2,3}$ and P $L_{2,3}$-edges

Three reference Ca-phosphate reference compounds were used to calibrate this method: MCPM (Ca/P = 0.5), DCPA (Ca/P = 1), and α-TCP (Ca/P = 1.5). For each reference compound, linear background-corrected spectra at the P and Ca $L_{2,3}$-edge spectra were used (Fig. 3A). According to the Beer-Lambert law, the height of the step measured at approximately 144 eV (h_P) in P $L_{2,3}$-edge spectra is proportional to the amount of P in the probed volume. Similarly, the height of the edge step of Ca at 360 eV (h_{Ca}) is proportional to the Ca amount in the same probed volume (Fig. 3C). Therefore, the parameter $R_{Ca/P}$, defined as: $R_{Ca/P} = h_{Ca}/h_P$ is proportional to the molar Ca/P ratio of a compound with a y-intercept of 0. In order to retrieve the factor of proportionality, $R_{Ca/P}$ was measured on ~1500 to ~9000 pixels for each of the four reference compounds. The mean $R_{Ca/P}$ ratios thus obtained for the four reference compounds were plotted *vs.* their molar Ca/P ratios (Fig. 4). A linear correlation was obtained between Ca/P molar rations and $R_{Ca/P}$, with a correlation coefficient of 0.97, and following this equation: Ca/P = 0.8895 x $R_{Ca/P}$. The residual standard error of the regression was ±0.15.

3.2 XANES spectroscopy of apatites at the Ca $L_{2,3}$- and C K-edges

A number of important naturally occurring Ca-phosphate-based materials belong to the apatite family. Specific XANES signatures at the Ca $L_{2,3}$-edges resulting from the CO_3^{2-} substitutions in apatite and associated alterations of crystallinity have been suggested by previous studies [33,47]. As biological materials are often intimately associated with an organic matrix, the determination of the C/Ca ratio does not provide a strict estimation of the

carbonate contents of these materials. However, carbonate functional groups can be efficiently detected, distinguished from organic carbon functional groups and specifically quantified by STXM at the C K-edge, using the peak at ~290.2 eV, which corresponds to 1s → π* electronic transitions in carbonate groups [72–74]. We focused here on apatitic compounds with the aim of developing an approach to assess their carbonate content.

3.2.1 XANES spectra of reference compounds and test samples at the C K- and Ca $L_{2,3}$-edges

The C*/Ca weight ratios (C* referring to C atoms in carbonate functional groups) of the different reference compounds used in this study (CHA 1, CHA 2 and CFA) were calculated using the chemical data provided in Section 2.2, and are 0.012, 0.028 and 0.036 for CHA 1, CHA 2 and CFA, respectively.

Fig. 5 shows the XANES spectra at the C K-edge and Ca $L_{2,3}$-edges of the three reference compounds used in this study as well as two test samples with unknown carbonate concentrations (a tooth and a bone). They were normalized to the same height of the Ca edge step at 360 eV. The peak corresponding to the 1s → π* transitions in carbonate groups (at ~290.1-290.2 eV) is the main peak in XANES spectra at the C K-edge for all reference compounds and test samples. Small peaks at 284.8 eV and 288.1 eV and a shoulder at 287.1 eV are also systematically present. They correspond to electronic transitions in organic C functional groups, respectively 1s → π* transitions in aromatics, 1s→π* transitions in amides (*e.g.* peptide groups in proteins) and 1s → π* transitions in phenols and ketones [72–76]. Their presence in the spectra of CHA 1 and 2, which were synthesized inorganically, suggests that some contamination by organic molecules occurred during sample preparation. XANES spectra of the bone sample presents a much stronger signal at the C K-edge than the reference compounds and other test samples, with a large peak at 288.2 eV and an additional peak at 289.4 eV. Bones typically have high organic contents (typically ~20 wt%, which can be

compared with the low organic content of mature enamel of ~0.1%), mostly as Type 1 collagen [1]. The peak at 289.4 eV it is often attributed to 1s→3p/σ* electronic transitions in alcohols [73,76] and may result from the presence of hydroxylated amino-acids in collagen [77].

3.2.2 **Rationale for CO_3/Ca quantification by STXM**

Linear background-corrected spectra at the Ca $L_{2,3}$-edges and C K-edges were used here (Fig. 6). $R_{CO3/Ca}$ is the ratio between the intensity of the peak corresponding to carbonate groups (at 290.2 eV) (*i.e.*, the absorption at 290.2 minus the absorption just after the peak at 291 eV) and the height of the Ca edge step at 360 eV. It is calculated as: $R_{CO3/Ca} = (OD_{290.2} - OD_{291})/OD_{360}$, where OD_x is the optical density value at x eV. $R_{CO3/Ca}$ was measured for ~900-3100 pixels for each sample.

We plotted $R_{CO3/Ca}$ *vs.* the C*/Ca weight ratio for the reference compounds (Fig. 7). The Beer-Lambert law predicts a linear relation with a y-intercept of 0. The relationship between $R_{CO3/Ca}$ and C*/Ca could thus be retrieved with the following equation: (C*/Ca)(wt% ratio) = 0.030 x $R_{CO3/Ca}$. The coefficients of correlation R^2 was ~0.97. The residual standard error of the regression was ±0.0018.

We used this relation to determine the C*/Ca weight ratios and the carbonate contents (by multiplying C*/Ca by Ca concentration in wt%) of the two test samples. The teeth had a C*/Ca weight ratio of ~0.02 (±9%) and a carbonate content of ~0.72 wt% C, and the bone had a C*/Ca weight ratio of ~0.03 (±6%) and a carbonate content of ~0.73 wt% C. These values are within the range of typical carbonate contents for bone and teeth minerals as provided by Elliott [1].

3.3 Case study: STXM analyses of a bone-like collagen/apatite matrix at the C K- and the Ca $L_{2,3}$-edges

Figure 9 illustrates the use of STXM/XANES to characterize and map Ca-phosphates in biological materials. The sample is composed of Ca-phosphate precipitated on a collagen matrix (Coll/CHA/SBF, [40]) and was mapped by STXM at the C K- and Ca $L_{2,3}$-edges with a ~25 nm spatial resolution (Fig. 9 A-D). Individual collagen fibrils, measuring ~80 nm in diameter, as well as the Ca-phosphate precipitates (50-300 nm) are visible. XANES spectra at the C K- and Ca $L_{2,3}$-edges have been obtained on these precipitates. Spectra at the Ca $L_{2,3}$-edges obtained on different grains were identical, showing that a single Ca-phosphate phase has precipitated in the collagen matrix. The average spectrum shown in Fig. 9 F is similar to the spectrum of the reference HA (Fig. 1), confirming that the precipitates have an apatitic structure. The C K-edge spectrum (Fig. 9 E) is similar to the C K-edge spectra of collagen obtained by x-ray photoemission electron spectromicroscopy (X-PEEM/XANES) by Lam et al. [78], with two sharp peaks at 285.1 eV and 288.5 eV, assigned respectively to 1s $\rightarrow \pi^*$ electronic transitions in C=C bounds and 1s $\rightarrow \pi^*$ transitions in carbonyl (C=O) groups, and a shoulder at 287.2 eV, assigned to 1s $\rightarrow \sigma^*$ transitions is C–H bounds [78]. An additional peak at 290.2 eV (1s $\rightarrow \pi^*$ transitions in carbonate groups), indicated by an arrow in Fig. 9 E, shows that the apatite precipitates are carbonated, confirming bulk FTIR analyses performed by Wang et al. [40] on the same sample. The $R_{CO3/Ca}$ ratio of this apatite as calculated using the method described in the previous section is ~0.19, corresponding to a C*/Ca ratio of 0.005 (±30%). No large spatial variations of this ratio were detected in the analyzed area. The calculated C*/Ca ratio is very low with a higher error bar but the peak at 290.2 eV, which is characteristic of carbonates, is clearly significant (Fig. 9) and this overall demonstrates the low detection limit of STXM for carbonates.

4 Discussion

4.1 Fingerprinting of Ca-phosphate biological materials using STXM/XANES at the Ca $L_{2,3}$- and P $L_{2,3}$-edges

4.1.1 Fingerprinting of Ca-phosphate biological materials using XANES spectra at the Ca and/or P $L_{2,3}$-edges

As described in section 3.1.1, XANES spectra of Ca-phosphate-based materials (mainly differences in the positions and intensities of minor peaks) can be used as probes of the local geometry and electronic structure of Ca in these phases (Fig. 1, Table 2). Besides its imaging capabilities at high spatial resolution (~25 nm), the main advantage of STXM/XANES over bulk methods such as XRD, FTIR or RMN is the possibility to obtain structural information on very small quantities of sample. Indeed, the investigated area in our case study (Fig. 9) is only a few micrometers in width, and XANES spectra at the Ca $L_{2,3}$-edges obtained on precipitates measuring only a few tens of nanometers could be used to demonstrate their apatitic structure.

Previous studies have shown the feasibility of using such specific fingerprints for micrometer to nanometer-scale mapping of different Ca-phosphate phases in biological materials. For example, Benzerara et al. used STXM/XANES at the Ca $L_{2,3}$-edges and the C K-edge to identify CHA among other candidate phases as the mineral formed by *Caulobacter crescentus* cells cultured in the presence of high calcium concentrations (8 mM) [72]. More recently, Beniash et al. used X-PEEM/XANES at the Ca $L_{2,3}$-edges to compare to characterize and map newly formed enamel minerals at different stages of maturation, and demonstrated that the phase formed at an early stage of enamel mineralization is ACP, which then transforms into CHA [33].

Ca-phosphates can be further characterized at the submicrometer-scale by STXM using XANES spectroscopy at the P $L_{2,3}$ edges. P $L_{2,3}$-edges XANES spectra of Ca-phosphates and polyphosphates indeed present distinctive features which can be used for fingerprinting these different species (see Section 3.1.2 and Fig. 2). The spectra of MPCM, DCPA, DCPD, CPP, α-TCP, β-TCP and HA shown here and acquired by STXM were very similar to those obtained previously by Kruse et al. [50] and Demirkiran et al. [49] at the bulk scale, showing the possibility to perform these analyses at the ~25 nm-scale. XANES P $L_{2,3}$-edge spectroscopy has been used to study the nature of Ca-phosphates present in ceramics used for restoration of damaged bone tissues [49]. P K-edge x-ray fluorescence spectro-microscopy was used to identify apatite and polyphosphates in marine sediments and map their association with a sub-micrometer-scale spatial resolution, supporting the importance of polyphosphates in sedimentary formation of apatite [9,67]. Applying P $L_{2,3}$-edges STXM/XANES spectro-microscopy for fingerprinting Ca-phosphates in such environmental samples at a higher spatial resolution is an exciting and yet unexplored area.

4.1.2 Fingerprinting of Ca-phosphate biological materials using Ca/P ratios

We have shown that Ca/P ratios of Ca-phosphate biological materials can be measured using STXM/XANES at the Ca and P $L_{2,3}$-edges, with an error of ±0.15. This can be performed down to the ~25 nm-scale. As stated in the introduction, Ca/P ratios can be used for fingerprinting Ca-phosphates. Mapping Ca-phosphates based on their whole Ca or P $L_{2,3}$-edges spectra requires using stacks, which can be time-consuming. The method described in Section 3.1.3 requires the acquisition of only six images: two images in the P $L_{2,3}$ pre-edge region and two images in the Ca $L_{2,3}$ pre-edge region for linear background removal, one image at 144 eV and one image at 360 eV, allowing relatively fast mapping of Ca/P ratios while maintaining good spatial resolution. Although Ca/P ratio can be determined more

accurately with bulk chemical methods, STXM offers the possibility to map variations of this ratio in a sample at the 25 nm-scale.

4.2 Assessing carbonate content of apatitic biological materials using STXM/XANES at the C K- and Ca $L_{2,3}$-edges

The incorporation of carbonates in apatites greatly influences their physical and chemical properties (*e.g.*, [3]). Incorporation of CO_3^{2-} ions in apatite and their distribution in A- and B-type sites are usually assessed by bulk techniques such as x-ray diffraction, Fourier-transform infrared (FTIR) and nuclear magnetic resonance (NMR) (*e.g.*, [1,27,28,54]). High resolution transmission electron microscopy (HRTEM) and electron diffraction do not allow for the detection of CO_3^{2-} substitution in apatites (*i.e.*, electron diffraction pattern of CHA are similar to those of pure HA; [42,79,80]). Moreover, CO_3^{2-} groups in apatites are difficult to map by TEM-EDXS when they are mixed with organic carbon, as is often the case in biological materials. Figure 9 shows that STXM on the other hand allows the detection of CO_3^{2-} groups in apatites even within an organic matrix. STXM moreover provide some information on the composition of organic matrix associated with the precipitates. In section 2.2.3, a STXM/XANES-based method is proposed allowing specific quantification and mapping of carbonates in apatites at the 25-nm scale, even when organic carbon is present.

Increased carbonate contents in apatites are generally associated with decreased crystallinity [22–24]. The replacement of PO_4^{3-} groups by CO_3^{2-}in nanosized apatites moreover leads to (i) the development of an ACP-like hydrated disorder surface layer at the expense of the crystalline apatitic core, and (ii) a decrease in the crystallites size [81]. Beniash et al. [33] compared XANES spectra at the Ca $L_{2,3}$-edges of HA, low crystallinity HA and ACP and found that the position of peak d_3 (at ~348.5 eV) was sensitive to crystallinity, appearing at lower energy in crystalline compared to amorphous phases. This finding is not

confirmed by our analyses. Indeed, the position of this peak for CHA 2 is slightly shifted towards lower energies compared to CHA 1 (Fig. 8), while CHA 2 contains more carbonate than CHA 1 (~2.2 wt% CO_3^{2-} for CHA 1 *vs.* ~4.9 wt% CO_3^{2-} for CHA 2). The peak at ~348.5 eV also occurs at lower energies in the tooth and the bone sample spectra compared to the CHA 1 spectra, which according to Beniash et al. [33] would indicate a relatively higher crystallinity, in disagreement with higher carbonate contents. This suggests that either (i) the crystallinity of these compounds is not controlled by carbonate content only (but also for instance by crystallite size), or (ii) the position of peak d_3 is influenced by other parameters than crystallinity.

CO_3^{2-} ions in carbonate apatites can be located in the *c*-axis channels of apatite (A-site) or they can substitute for tetrahedral PO_4^{3-} groups (B-site) [17]. Fleet and Liu [47] compared the Ca $L_{2,3}$-edges XANES spectra of synthetic A-type carbonate hydroxyapatites. They found that the only feature characteristic of the presence of CO_3^{2-} was the weak intensity of peak b_3 (at ~347.6 eV). This was interpreted as a change of Ca coordination due to the presence of CO_3^{2-} in the apatite channels. Here, we observe that the intensity of peak b_3 is quite similar in the spectra of the different reference compounds and test samples. CO_3^{2-} ions are mainly present in B-sites in CHA 1 and 2 according to Nassif et al. [54]. It has been shown by FTIR and MAS NMR studies that most CO_3^{2-} groups (~75 %) in sedimentary CFA occupy the B-sites (*e.g.*, [28,82]), and it is also known that carbonate anions mainly substitute for PO_4^{3-} (B-sites) in the mineral phase of bones [1]. However, Yi et al. [58] have shown that a significant portion of CO_3^{2-} ions are present in A-sites in the tooth samples studied here. The relationship between the presence of A-type carbonates in apatites and b_3 peak intensity proposed by Fleet and Liu [47] therefore does not apply here.

The influence of carbonate substitution on the XANES spectra at the Ca $L_{2,3}$-edges of apatites therefore requires further investigation. Simulation of experimental Ca $L_{2,3}$-edges

XANES spectra of different types of Ca-carbonates using multiplet calculations is an effective method to provide information about the local coordination of Ca in these biological materials [83]. This approach therefore appears promising to gain further understanding in the interpretation of apatites spectra at the XANES $L_{2,3}$-edges.

5 Conclusion

This study shows the feasibility of identifying and mapping Ca-phosphate minerals as well as important parameters relevant to biomineralization studies such as the Ca/P ratio and carbonate content of these phases at the sub-micrometer scale. Unlike bulk methods such as XRD, FTIR or NRM, STXM requires minimal amounts of samples, and offers imaging capabilities. STXM is moreover quite unique in allowing the detection, mapping (at the ~25 nm scale) and quantification of carbonate groups in apatite minerals embedded in an organic matrix.

The Ca-phosphate fingerprinting methods presented here can be applied to a diversity of studies dealing with biological materials formation. An interesting potential application is the characterization of Ca-phosphate mixtures in such materials. For instance, apatite composing the mineral fraction of bones and teeth is thought to precipitate via the formation of other non-apatitic Ca-phosphate precursor phases [33,34,29,35]. As a consequence, mixtures of mature apatite and precursor phases resulting from the incomplete transformation of the transient phases to apatite, or the co-precipitation of apatite with other Ca-phosphates, may occur in such materials. Cements used for bone and tooth implants are also very often composed of mixtures of Ca-phosphates (*e.g.*, [84–86]), and HA sometimes co-exists with other Ca-phosphate phases in pathologic calcifications [30,87,88]. Few studies have dealt with the characterization of Ca-phosphates mixtures despite the abundance of such mixtures in natural systems ([25] and references therein). STXM/XANES is a promising method for the

sub-micrometer scale characterization of Ca-phosphates mixtures, with potential to improve our understanding on the formation mechanisms of these materials.

Acknowledgments

We thank Florence Babonneau, Yan Wang, Stanislas Von Euw, Christian Bonhomme and Frédérique Pourpoint (Collège de France and UPMC, Paris), for giving some of the reference Ca-phosphates used in this study. Haohao Yi and Etienne Balan (IMPMC, Paris), are also thanked for providing compounds and analyses. We gratefully acknowledge support from the Simone and Cino Del Duca Fundation for the funding of JC salary. Part of the research leading to these results has received funding from the European Research Council under the European Community's Seventh Framework Programme (FP7/2007-2013 Grant Agreement no.307110 - ERC CALCYAN). Advanced Light Source (ALS) Molecular Environmental Science beamline 11.0.2 is supported by the Office of Science, Office of Basic Energy Sciences, Division of Chemical Sciences, Geosciences, and Biosciences and Materials Sciences Division, U.S. Department of Energy, at the Lawrence Berkeley National Laboratory. Beamline 10ID-1 at the CLS, is supported by the NSERC, the CIHR, the NRC, and the University of Saskatchewan. We thank Chithra Karunakaran and Jian Wang for their support of the STXM at the CLS. The authors are indebted to Hannah Miller (University of Colorado) for proofreading this article.

References

[1] Elliott JC. Calcium Phosphate Biominerals. Rev Mineral Geochem 2002;48:427–53.

[2] Rey C, Combes C, Drouet C, Glimcher MJ. Bone mineral: update on chemical composition and structure. Osteoporos Int 2009;20:1013–21.

[3] Wopenka B, Pasteris JD. A mineralogical perspective on the apatite in bone. Mater Sci Eng C 2005;25:131–43.

[4] Bazin D, Daudon M, Combes C, Rey C. Characterization and Some Physicochemical Aspects of Pathological Microcalcifications. Chem Rev 2012;112:5092–120.

[5] Crosby CH, Bailey JV. The role of microbes in the formation of modern and ancient phosphatic mineral deposits. Front Microbiol 2012;3:241.

[6] Follmi K. The phosphorus cycle, phosphogenesis and marine phosphate-rich deposits. Earth-Sci Rev 1996;40:55–124.

[7] Brown MRW. Inorganic polyphosphate in the origin and survival of species. Proc Natl Acad Sci 2004;101:16085–7.

[8] Kornberg A. Inorganic polyphosphate: toward making a forgotten polymer unforgettable. J Bacteriol 1995;177:491–6.

[9] Diaz J, Ingall E, Benitez-Nelson C, Paterson D, de Jonge MD, McNulty I, et al. Marine Polyphosphate: A Key Player in Geologic Phosphorus Sequestration. Science 2008;320:652–5.

[10] Schulz HN, Schulz HD. Large Sulfur Bacteria and the Formation of Phosphorite. Science 2005;307:416–8.

[11] Omelon SJ, Grynpas MD. Relationships between Polyphosphate Chemistry, Biochemistry and Apatite Biomineralization. Chem Rev 2008;108:4694–715.

[12] Bohner M. Calcium orthophosphates in medicine: from ceramics to calcium phosphate cements. Injury 2000;31 Suppl 4:37–47.

[13] Dorozhkin SV. Nanodimensional and Nanocrystalline Apatites and Other Calcium Orthophosphates in Biomedical Engineering, Biology and Medicine. Materials 2009;2:1975–2045.

[14] Liou S-C, Chen S-Y, Lee H-Y, Bow J-S. Structural characterization of nano-sized calcium deficient apatite powders. Biomaterials 2004;25:189–96.

[15] Pan H-B, Darvell BW. Calcium Phosphate Solubility: The Need for Re-Evaluation. Cryst Growth Des 2009;9:639–45.

[16] Meyer JL, Fowler BO. Lattice defects in nonstoichiometric calcium hydroxylapatites. A chemical approach. Inorg Chem 1982;21:3029–35.

[17] Pan Y, Fleet ME. Compositions of the Apatite-Group Minerals: Substitution Mechanisms and Controlling Factors. Rev Mineral Geochem 2002;48:13 –49.

[18] Pan H, Darvell BW. Effect of Carbonate on Hydroxyapatite Solubility. Cryst Growth Des 2010;10:845–50.

[19] Fulmer MT, Ison IC, Hankermayer CR, Constantz BR, Ross J. Measurements of the solubilities and dissolution rates of several hydroxyapatites. Biomaterials 2002;23:751–5.

[20] Hankermeyer CR, Ohashi KL, Delaney DC, Ross J, Constantz BR. Dissolution rates of carbonated hydroxyapatite in hydrochloric acid. Biomaterials 2002;23:743–50.

[21] Harries JE, Hasnain SS, Shah JS. EXAFS study of structural disorder in carbonate-containing hydroxyapatites. Calcif Tissue Int 1987;41:346–50.

[22] Harries JE, Hukins DWL, Hasnain SS. Calcium environment in bone mineral determined by EXAFS spectroscopy. Calcif Tissue Int 1988;43:250–3.

[23] Vignoles M, Bonel G, Holcomb DW, Young RA. Influence of preparation conditions on the composition of type B carbonated hydroxyapatite and on the localization of the carbonate ions. Calcif Tissue Int 1988;43:33–40.
[24] Xu C, Reed R, Gorski JP, Wang Y, Walker MP. The distribution of carbonate in enamel and its correlation with structure and mechanical properties. J Mater Sci 2012;47:8035–43.
[25] Karampas IA, Kontoyannis CG. Characterization of calcium phosphates mixtures. Vib Spectrosc 2013;64:126–33.
[26] Vallet-regi M, Rodriguez-Lorenzo LM, Salinas AJ. Synthesis and characterisation of calcium deficient apatite. Solid State Ion 1997;101-103:1279–85.
[27] Fleet ME, Liu X, King PL. Accommodation of the carbonate ion in apatite: An FTIR and X-ray structure study of crystals synthesized at 2–4 GPa. Am Mineral 2004;89:1422–32.
[28] Yi H, Balan E, Gervais C, Segalen L, Fayon F, Roche D, et al. A carbonate-fluoride defect model for carbonate-rich fluorapatite. Am Mineral 2013;98:1066–9.
[29] Crane NJ, Popescu V, Morris MD, Steenhuis P, Ignelzi MA Jr. Raman spectroscopic evidence for octacalcium phosphate and other transient mineral species deposited during intramembranous mineralization. Bone 2006;39:434–42.
[30] Chen K-H, Li M-J, Cheng W-T, Balic-Zunic T, Lin S-Y. Identification of monoclinic calcium pyrophosphate dihydrate and hydroxyapatite in human sclera using Raman microspectroscopy. Int J Exp Pathol 2009;90:74–8.
[31] Cho G. Detection of Hydroxyl Ions in Bone Mineral by Solid-State NMR Spectroscopy. Science 2003;300:1123–7.
[32] Wang Y, Von Euw S, Fernandes F, Cassaignon S, Selmane M, Laurent G, Pehau-Arnaudet G, Coelho C, Bonhomme-Coury L, Giraud-Guille M-M, Babonneau F, Azaïs T, Nassif N. Water-mediated structuring of bone apatite. Nature Mater 2013;12:1244-1153.
[33] Beniash E, Metzler RA, Lam RSK, Gilbert PUPA. Transient amorphous calcium phosphate in forming enamel. J Struct Biol 2009;166:133–43.
[34] Mahamid J, Aichmayer B, Shimoni E, Ziblat R, Li C, Siegel S, et al. Mapping amorphous calcium phosphate transformation into crystalline mineral from the cell to the bone in zebrafish fin rays. Proc Natl Acad Sci 2010;107:6316–21.
[35] Weiner S. Transient precursor strategy in mineral formation of bone. Bone 2006;39:431–3.
[36] Grynpas MD, Omelon S. Transient precursor strategy or very small biological apatite crystals? Bone 2007;41:162–4.
[37] Arnold S, Plate U, Wiesmann HP, Stratmann U, Kohl H, Höhling HJ. Quantitative analyses of the biomineralization of different hard tissues. J Microsc 2001;202:488–94.
[38] Leng Y, Chen J, Qu S. TEM study of calcium phosphate precipitation on HA/TCP ceramics. Biomaterials 2003;24:2125–31.
[39] Lu X, Leng Y. TEM study of calcium phosphate precipitation on bioactive titanium surfaces. Biomaterials 2004;25:1779–86.
[40] Wang Y, Azaïs T, Robin M, Vallée A, Catania C, Legriel P, et al. The predominant role of collagen in the nucleation, growth, structure and orientation of bone apatite. Nat Mater 2012;11:724–33.
[41] Xin R, Leng Y, Chen J, Zhang Q. A comparative study of calcium phosphate formation on bioceramics in vitro and in vivo. Biomaterials 2005;26:6477–86.
[42] Xin R, Leng Y, Wang N. HRTEM Study of the Mineral Phases in Human Cortical Bone. Adv Eng Mater 2010;12:B552–B557.

[43] Eddisford P, Brown A, Brydson R. Identifying and quantifying the mechanism of electron beam induced damage and recovery in hydroxyapatite. J Phys Conf Ser 2008;126:012008.
[44] Braun A, Huggins FE, Shah N, Chen Y, Wirick S, Mun SB, et al. Advantages of soft X-ray absorption over TEM-EELS for solid carbon studies—a comparative study on diesel soot with EELS and NEXAFS. Carbon 2005;43:117–24.
[45] Hitchcock AP, Dynes JJ, Johansson G, Wang J, Botton G. Comparison of NEXAFS microscopy and TEM-EELS for studies of soft matter. Micron Oxf Engl 1993 2008;39:311–9.
[46] Cosmidis J, Benzerara K. Soft X-ray Scanning Transmission Spectromicroscopy. Biomineralization Sourcebook: Characterization of Biominerals and Biomimetic Materials, London, UK: E. DiMasi and L.B. Gower; 2014.
[47] Fleet ME, Liu X. Calcium L2,3-edge XANES of carbonates, carbonate apatite, and oldhamite (CaS). Am Mineral 2009;94:1235–41.
[48] Naftel SJ, Sham TK, Yiu YM, Yates BW. Calcium L-edge XANES study of some calcium compounds. J Synchrotron Radiat 2001;8:255–7.
[49] Demirkiran H, Hu Y, Zuin L, Appathurai N, Aswath PB. XANES analysis of calcium and sodium phosphates and silicates and hydroxyapatite–Bioglass®45S5 co-sintered bioceramics. Mater Sci Eng C 2011;31:134–43.
[50] Kruse J, Leinweber P, Eckhardt K-U, Godlinski F, Hu Y, Zuin L. Phosphorus $L_{2,3}$ -edge XANES: overview of reference compounds. J Synchrotron Radiat 2009;16:247–59.
[51] Pourpoint F, Gervais C, Bonhomme-Coury L, Azaïs T, Coelho C, Mauri F, et al. Calcium Phosphates and Hydroxyapatite: Solid-State NMR Experiments and First-Principles Calculations. Appl Magn Reson 2007;32:435–57.
[52] Pourpoint F, Kolassiba A, Gervais C, Azaïs T, Bonhomme-Coury L, Bonhomme C, et al. First Principles Calculations of NMR Parameters in Biocompatible Materials Science: The Case Study of Calcium Phosphates, β- and γ-$Ca(PO_3)_2$. Combination with MAS-J Experiments. Chem Mater 2007;19:6367–9.
[53] Pourpoint F. Etude structurale de phosphates de calcium par une approche combinée entre RMN à l'état solide et calculs ab initio. Thesis manuscript. Université Pierre et Marie Curie, 2009.
[54] Nassif N, Martineau F, Syzgantseva O, Gobeaux F, Willinger M, Coradin T, et al. In Vivo Inspired Conditions to Synthesize Biomimetic Hydroxyapatite. Chem Mater 2010;22:3653–63.
[55] Cosmidis J, Benzerara K, Gheerbrant E, Estève I, Bouya B, Amaghzaz M. Nanometer-scale characterization of exceptionally preserved bacterial fossils in Paleocene phosphorites from Ouled Abdoun (Morocco). Geobiology 2013;11:139–53.
[56] Schuffert J., Kastner M, Emanuele G, Jahnke R. Carbonate-ion substitution in francolite: A new equation. Geochim Cosmochim Acta 1990;54:2323–8.
[57] Yi H, Balan E, Gervais C, Ségalen L, Roche D, Person A, et al. Probing atomic scale transformation of fossil dental enamel using Fourier transform infrared and nuclear magnetic resonance spectroscopy: A case study from the Tugen Hills (Rift Gregory, Kenya). Acta Biomater 2014.
[58] Yi H. Cristallochimie des apatites biologiques et géologiques : Marqueurs minéralogiques de la fossilisation. Thesis manuscript. Université Pierre et Marie Curie, 2013.
[59] Bluhm H, Andersson K, Araki T, Benzerara K, Brown GE, Dynes JJ, et al. Soft X-ray microscopy and spectroscopy at the molecular environmental science beamline at the Advanced Light Source. J Electron Spectrosc Relat Phenom 2006;150:86–104.
[60] Kaznatcheev KV, Karunakaran C, Lanke UD, Urquhart SG, Obst M, Hitchcock AP. Soft X-ray spectromicroscopy beamline at the CLS: Commissioning results. Nucl

Instrum Methods Phys Res Sect Accel Spectrometers Detect Assoc Equip 2007;582:96–9.

[61] Bourdelle F, Benzerara K, Beyssac O, Cosmidis J, Neuville DR, Brown GE, et al. Quantification of the ferric/ferrous iron ratio in silicates by scanning transmission X-ray microscopy at the Fe $L_{2,3}$ -edges. Contrib Mineral Petrol 2013.

[62] Hitchcock A. aXis2000 source. AXis2000—analysis X-Ray Images Spectra 2012.

[63] Hanhan S, Smith AM, Obst M, Hitchcock AP. Optimization of analysis of soft X-ray spectromicroscopy at the Ca 2p edge. J Electron Spectrosc Relat Phenom 2009;173:44–9.

[64] Carrodeguas RG, De Aza S. α-Tricalcium phosphate: Synthesis, properties and biomedical applications. Acta Biomater 2011;7:3536–46.

[65] Yashima M, Sakai A, Kamiyama T, Hoshikawa A. Crystal structure analysis of β-tricalcium phosphate $Ca_3(PO_4)_2$ by neutron powder diffraction. J Solid State Chem 2003;175:272–7.

[66] Wetherall KM, Pickup DM, Newport RJ, Mountjoy G. The structure of calcium metaphosphate glass obtained from x-ray and neutron diffraction and reverse Monte Carlo modelling. J Phys Condens Matter 2009;21:035109.

[67] Brandes JA, Ingall E, Paterson D. Characterization of minerals and organic phosphorus species in marine sediments using soft X-ray fluorescence spectromicroscopy. Mar Chem 2007;103:250–65.

[68] Ingall ED, Brandes JA, Diaz JM, de Jonge MD, Paterson D, McNulty I, et al. Phosphorus *K* -edge XANES spectroscopy of mineral standards. J Synchrotron Radiat 2010;18:189–97.

[69] Shober AL, Hesterberg DL, Sims JT, Gardner S. Characterization of Phosphorus Species in Biosolids and Manures Using XANES Spectroscopy. J Environ Qual 2006;35:1983.

[70] Siritapetawee J, Pattanasiriwisawa W. An attempt at kidney stone analysis with the application of synchrotron radiation. J Synchrotron Radiat 2008;15:158–61.

[71] Wang C, Eisa MH, Jin W, Shen H, Mi Y, Gao J, et al. Age-related elemental change in bones. Nucl Instrum Methods Phys Res Sect B Beam Interact Mater At 2008;266:1619–22.

[72] Benzerara K, Yoon TH, Tyliszczak T, Constantz B, Spormann AM, Brown GE. Scanning transmission X-ray microscopy study of microbial calcification. Geobiology 2004;2:249–59.

[73] Brandes JA, Lee C, Wakeham S, Peterson M, Jacobsen C, Wirick S, et al. Examining marine particulate organic matter at sub-micron scales using scanning transmission X-ray microscopy and carbon X-ray absorption near edge structure spectroscopy. Mar Chem 2004;92:107–21.

[74] Schumacher M, Christl I, Scheinost AC, Jacobsen C, Kretzschmar R. Chemical Heterogeneity of Organic Soil Colloids Investigated by Scanning Transmission X-ray Microscopy and C-1s NEXAFS Microspectroscopy. Environ Sci Technol 2005;39:9094–100.

[75] Haberstroh PR, Brandes JA, Gélinas Y, Dickens AF, Wirick S, Cody G. Chemical composition of the graphitic black carbon fraction in riverine and marine sediments at sub-micron scales using carbon X-ray spectromicroscopy. Geochim Cosmochim Acta 2006;70:1483–94.

[76] Lehmann J, Liang B, Solomon D, Lerotic M, Luizão F, Kinyangi J, et al. Near-edge X-ray absorption fine structure (NEXAFS) spectroscopy for mapping nano-scale distribution of organic carbon forms in soil: Application to black carbon particles. Glob Biogeochem Cycles 2005;19.

[77] Gallop PM, Paz MA. Posttranslational protein modifications, with special attention to collagen and elastin. Physiol Rev 1975;55:418–87.
[78] Lam R, Metzler R, Gilbert P, Beniash E. Anisotropy chemical bounds in collagen molecules studied by X-ray absorption near-edge structure (XANES) spectroscopy. ACS Chem Biol 2012;7:476–480.
[79] Daculsi G, LeGeros RZ, Heughebaert M, Barbieux I. Formation of carbonate-apatite crystals after implantation of calcium phosphate ceramics. Calcif Tissue Int 1990;46:20–7.[80] Müller L, Conforto E, Caillard D, Müller FA. Biomimetic apatite coatings — Carbonate substitution and preferred growth orientation. Biomol Eng 2007;24:462–6.
[81] Wang Y, Von Euw S, Laurent G, Crevant C, Bonhomme-Coury L, Giraud-Guille M-M, Babonneau F, Nassif N, Azaïs T. Impact of collagen confinement vs. ionic substitutions on the local disorder in bone and biomimetic apatites. Mater Horizons 2013;1:224–231.
[82] Regnier P, Lasaga AC, Berner RA, Han OH, Zilm KW. Mechanism of CO_3^{2-} substitution in carbonate-fluorapatite; evidence from FTIR spectroscopy, ^{13}C NMR, and quantum mechanical calculations. Am Mineral 1994;79:809–18.
[83] Rez P, Blackwell A. Ca L23 Spectrum in Amorphous and Crystalline Phases of Calcium Carbonate. J Phys Chem B 2011;115:11193–8.
[84] Khashaba RM, Moussa M, Koch C, Jurgensen AR, Missimer DM, Rutherford RL, et al. Preparation, Physical-Chemical Characterization, and Cytocompatibility of Polymeric Calcium Phosphate Cements. Int J Biomater 2011;2011:1–13.
[85] Kim YB, Lee BM, Lee MC, Noh I, Lee S-J, Kim SS. Preparation and characterization of calcium phosphate cement of α-tricalcium phosphate-tetracalcium phosphate-dicalcium phosphate system incorporated with poly(γ-glutamic acid). Macromol Res 2013;21:892–8.
[86] Liou S-C, Chen S-Y, Liu D-M. Phase development and structural characterization of calcium phosphate ceramics-polyacrylic acid nanocomposites at room temperature in water-methanol mixtures. J Mater Sci Mater Med 2004;15:1261–6.
[87] Lin S-Y, Chen K-H, Li M-J, Cheng W-T, Wang S-L. Evidence of octacalcium phosphate and Type-B carbonated apatites deposited on the surface of explanted acrylic hydrogel intraocular lens. J Biomed Mater Res 2004;70B:203–8.
[88] Mikroulis D, Mavrilas D, Kapolos J, Koutsoukos PG, Lolas C. Physicochemical and microscopical study of calcific deposits from natural and bioprosthetic heart valves. Comparison and implications for mineralization mechanism. J Mater Sci Mater Med 2002;13:885–9.

Captions

Table 1. List of several calcium phosphate compounds (adapted from Elliott (2002) [1] and Dorozhkin (2009) [13]). Compounds indicated by an asterisk (*) have been analyzed in this study.

Table 2. Energy positions of the peaks in the Ca $L_{2,3}$-edge spectra of reference Ca-phosphate compounds. The numbers in brackets refer to energy positions of shoulders in the spectra.

Fig. 1. XANES at the Ca $L_{2,3}$-edges spectra of several Ca-phosphate reference compounds. Vertical dotted lines correspond to the peak energies of HA (see Table 2).

Fig. 2. P $L_{2,3}$-edges XANES spectra of reference Ca-phosphate compounds. Vertical dotted lines correspond to energy positions of the peaks in HA spectrum (136.7, 137.6, 138.4, 139.0, 142.0 and 146.9 eV).

Fig. 3. (A) XANES spectrum of MCPM at the P and Ca $L_{2,3}$-edges before (black line) and after (grey line) performing linear background correction. (B) Linear background corrected spectrum at the P $L_{2,3}$-edges. The red arrow shows the positions of the edge step used for measuring $R_{Ca/P}$. (C) Linear background corrected spectrum at the Ca $L_{2,3}$-edges. The black arrow shows the position of the edge step used for measuring $R_{Ca/P}$.

Fig.4. Ca/P molar ratios *vs.* $R_{Ca/P}$ measured for MCPM, DCPA and α-TCP. Regression line and correlation coefficient (R^2) are shown. Error bars correspond to standard deviations for $R_{Ca/P}$ measurements on ~1500-9000 pixels.

Fig. 5. Linear background-corrected XANES spectra at the C K-edge (left) and Ca $L_{2,3}$-edges (right) of reference compounds and test samples. The position of the Ca L_2-edge has been

adjusted to 352.5 eV (vertical dotted line). The spectra have been divided by the height of the edge step at 360 eV.

Fig. 6. XANES spectrum of CFA at the C K-edge and Ca $L_{2,3}$-edges. Linear background correction has been performed at both C K and Ca $L_{2,3}$ edges. $R_{CO3/Ca}$ is calculated by measuring the height of the peak at 290.2 eV and the height of the Ca edge step at 360 eV (blue arrows).

Fig. 7. C*/Ca weight ratio (C* are C atoms present as carbonates) vs. $R_{CO3/Ca}$ measured for reference compounds CHA1, CHA2 and CFA. The regression line obtained and correlation coefficients (R^2) are shown. Error bars correspond to standard deviations for $R_{CO3/Ca}$ measurements on ~900-3100 pixels.

Fig. 8. Magnification of the Ca $L_{2,3}$ pre-edge region of the XANES spectra of reference compounds and test samples.

Fig. 9. STXM/XANES maps and spectra of apatite nanoparticules precipitated on a bone-like collagen matrix (Coll/CHA/SBF in [40]). (A) Image at 288.2eV. (B) Map of organic carbon obtained by subtracting an image at 280 eV (below the C K-edge) from an image at 288.2 eV (corresponding to 1s→π* electronic transition in amide groups). (C) Corresponding calcium map obtained by subtracting an image at 340 eV (below the Ca $L_{2,3}$-edge) from an image at 349.2 eV (corresponding the Ca L_3 edge). (B) and (C) were acquired on the same sub-area designated by a square on image (A). The pixel size on maps (B) and (C) is 20 nm. (D) Composite map obtained using (B) and (C), showing collagen fibers in red and calcium (apatite precipitates) in blue. (E) XANES spectrum at the C K edge obtained on apatite precipitates. Three main peaks are present at 284.8 eV (1s → π* transitions in aromatics), 288.2 eV (1s → π* transitions in amides) and 290.2 eV (1s → π* transitions in carbonates) (arrow). (F) XANES spectrum at the Ca $L_{2,3}$-edge obtained on apatite precipitates.

Fig. S1. XRD patterns of commercial Ca-phosphate compounds ACP, α-TCP and HA. Squares and circles correspond to reference ICDD patterns of HA (ICDD #09-0432) and α-TCP (ICDD #29-0359), respectively. All observed diffraction peaks relate to reference spectra and no impurity phases were found.

Fig. S2. Assessment of spectral distortions in XANES spectra at the Ca-$L_{2,3}$ edge due to absorption saturation effects. (A) Map at 349.2 eV of TTCP particles showing different ranges of absorption (in OD units). The different colors represent areas from which the spectra shown in (B) were extracted, corresponding to different OD ranges (*i.e.*, different thicknesses of the particles). (B) XANES spectra obtained on the different areas represented in (A), extracted using the Mask tool of aXis2000. It can be seen that some distortions of the spectra occur when the sample becomes too thick. (C) Plots of peak a_3 height (ha_3) *vs.* peak L_3 height (hL_3) for each pixel of the sample in (A). The dashed line corresponds to the ha_3/ $h(L_3)$ ratio obtained for pixels with a maximum OD (hL_3) <1. For thin areas of the sample, the ratio between ha_3 and hL_3 is roughly a constant. However, for thicker area (say, areas with OD >1.5), this ratio increases with the thickness of the sample, indicating variations in the relative heights of the peaks (pixels deviate from the dashed line at high maximum OD values, showing that the ha_3/ hL_3 ratio increases with increasing sample thickness). In order to avoid such spectral distortions, the spectra of the reference Ca-phosphate compounds were extracted from areas showing a maximum OD value <1 at 349.2 eV (energy position of the peak L_3). For example, only the purple and blue regions in (A) would be selected for the TTCP XANES spectra at the Ca $L_{2,3}$-edges.

Fig. S3. Ca $L_{2,3}$-edges XANES spectra processing. The black line is the measured spectrum of HA. First, a linear background background correction was applied to obtain the grey line, with 0 OD and a zero slope in the pre-edge region (340 to 345 eV). Second, a double arctan function (blue line) was subtracted to obtain the final spectrum (in red).

Name	Abbreviation	Formula	Ca/P
Polyphosphates*	PP	$M^{I}_{m}H_{(n+2)}P_nO_{(3n+1)}$ $M^{I} = Ca^{2+}, Na^{+}, Fe^{3+}, Fe^{2+},\ldots$	**ε**
Monocalcium phosphate monohydrate*	MCPM	$Ca(H_2PO_4)_2,H_2O$	**0.5**
Monocalcium phosphate anhydrous	MCPA	$Ca(H_2PO_4)_2$	**0.5**
Brushite, Dicalcium phosphate dihydrate*	DCPD	$CaHPO_4,2H_20$	**1.0**
Monetite, Dicalcium phosphate anhydrous*	DCPA	$CaHPO_4$	**1.0**
Calcium pyrophosphate (α, β or γ)	α-, β- or γ-CPP	$Ca_2P_2O_7$	**1.0**
Calcium pyrophosphate dihydrate	CPPD	$Ca_2P_2O_7,2H_2O$	**1.0**
Amorphous calcium phosphate *	ACP	$Ca_xH_y(PO4)_z,n(H_2O)$ (n=3-4.5)	**1.2-2.2**
Whitlockite		$Ca_{18}(Mg,Fe^{2+})_2H_2(PO_4)_{14}$	**1.29**
Octacalcium phosphate	OCP	$Ca_8H_2(PO_4)_6,5H_20$	**1.33**
Tricalcium phosphate (α or β)*	α- or β-TCP	$Ca_3(PO_4)_2$	**1.5**
Calcium-deficient hydroxyapatite	CDHA	$Ca_{10-x}(HPO_4)_x(PO_4)_{6-x}(OH)_{2-x}$ (0<x<1)	**1.4-1.67**
Hydroxyapatite	HA	$Ca_{10}(PO_4)_6(OH)_2$	**1.67**
Amorphous hydroxyapatite	HAa	$Ca_{10}(PO_4)_6(OH)_2,nH_2O$	**1.67**
Oxyapatite	OXA	$Ca_{10}(PO_4)_6O$	**1.67**
Fluoroapatite	FA	$Ca_{10}(PO_4)_6F_2$	**1.67**
Carbonate hydroxyapatite*	CHA	$Ca_{10-p}(PO_4)_{6-p}(OH)_{2-p}(CO_3)_p$ (0<p<1)	**>1.67**
Francolite, Carbonate-fluoroapatite*	CFA	$(Ca,Mg,Sr,Na)_{10}(PO_4,SO_4,CO_3)_6F_{2-3}$	**>1.67**
Hilgenstockite, Tetracalcium phosphate*	TTCP	$Ca_4(PO_4)_2O$	**2.0**

Compound	Energy positions (eV)
PP	347.9 349.3 351.2 352.5
MCPM	347.0 347.6 348.3 348.6 349.3 351.4 352.5
DCPD	347.1 (347.6) 348.2 348.6 349.2 351.4 352.5
DCPA	347.1 347.6 348.2 348.6 349.3 351.4 (351.8) 352.5
α-TCP	347.0 (347.6) 348.1 348.5 349.2 351.4 352.5
β-TCP	347.2 347.8 348.3 348.6 349.2 351.1 351.5 351.7 352.5
HA	347.0 (347.6) 348.1 348.5 349.2 (351.0) 351.4 351.8 352.5
TTCP	347.1 (347.9) 348.2 348.6 349.3 351.4 351.8 352.5

Figure 1

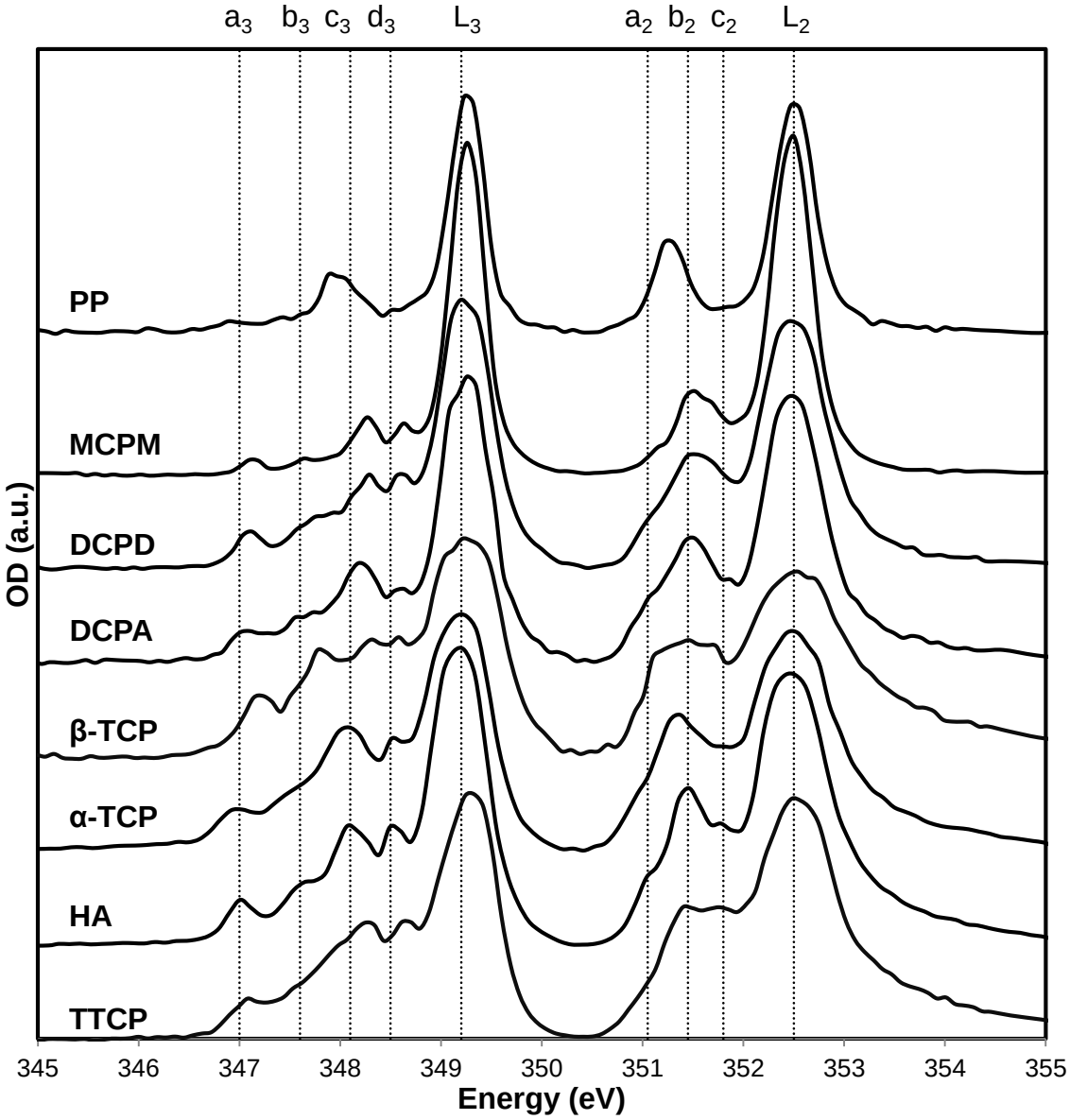
a3
b3
c3
d3
L3
a2
b2
c2
L2
PP
MCPM
DCPD
DCPA
β-TCP
α-TCP
HA
TTCP
OD (a.u.)
345
346
347
348
349
350
351
352
353
354
355
Energy (eV)

Figure 2

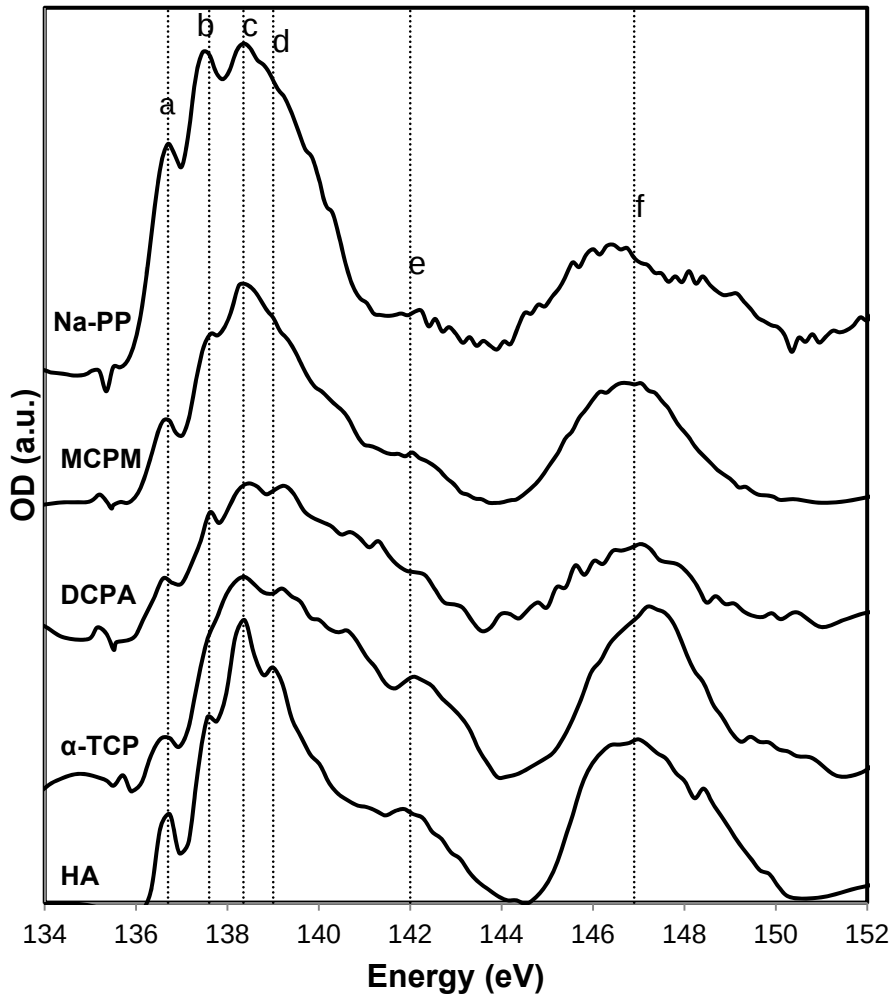

Figure 3

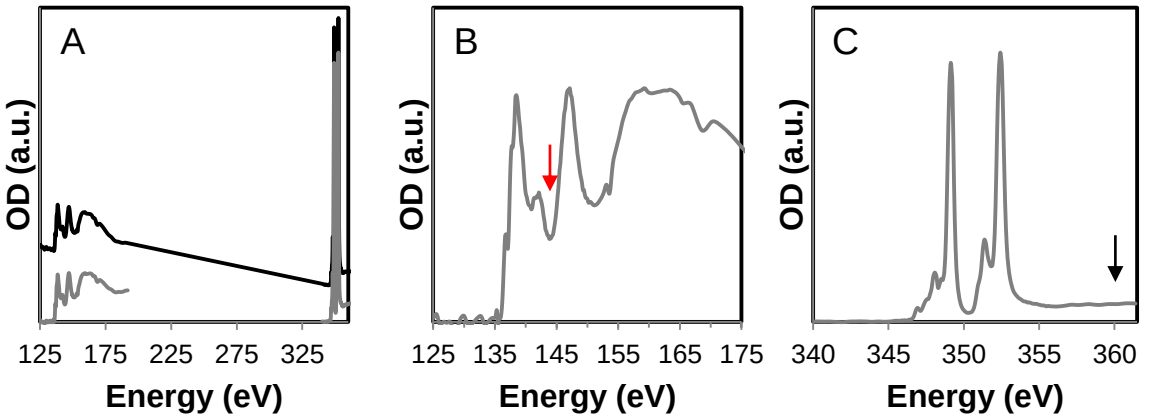
A
B
C
OD (a.u.)
OD (a.u.)
OD (a.u.)
125 175 225 275 325
Energy (eV)
125 135 145 155 165 175
Energy (eV)
340 345 350 355 360
Energy (eV)

Figure 4

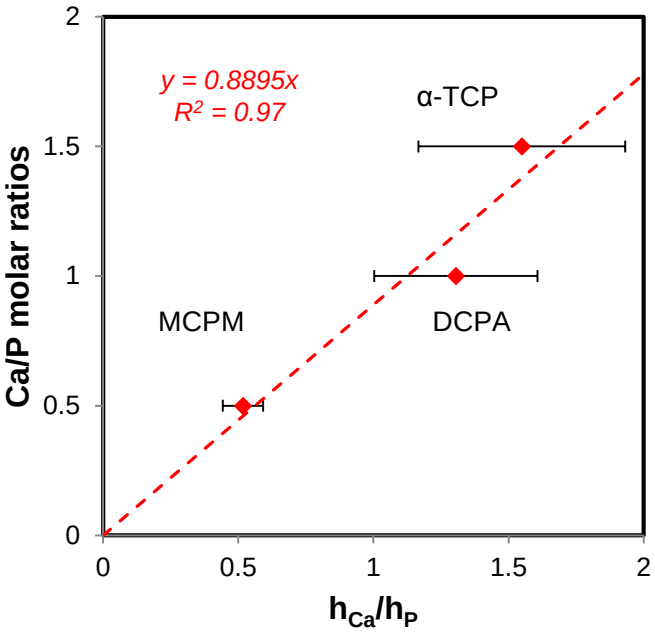
y = 0.8895x
R² = 0.97
α-TCP
MCPM
DCPA
Ca/P molar ratios
h_Ca/h_P
0
0.5
1
1.5
2

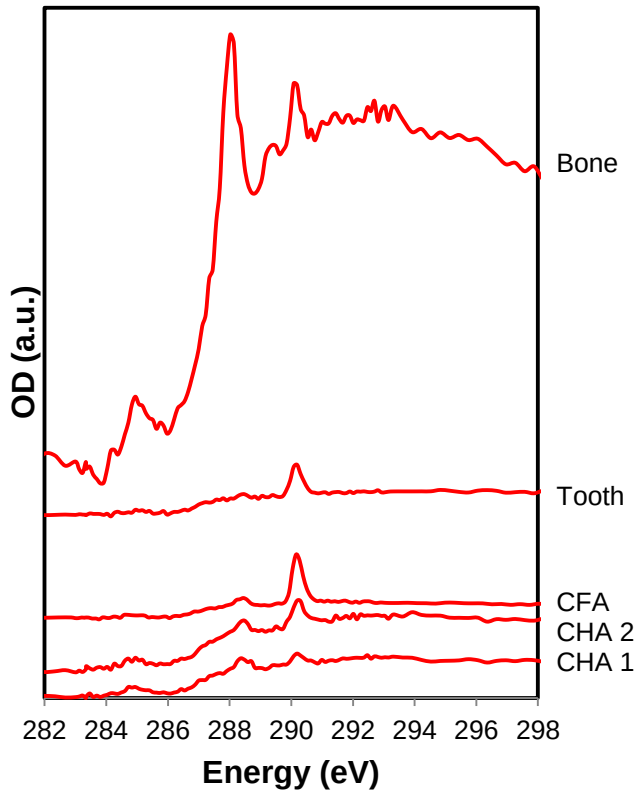
OD (a.u.)
Bone
Tooth
CFA
CHA 2
CHA 1
282 284 286 288 290 292 294 296 298
Energy (eV)

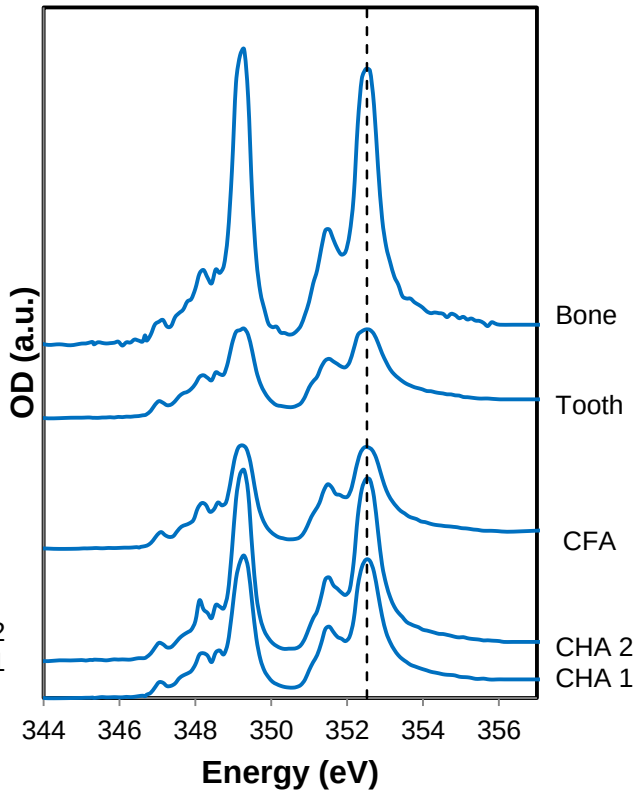
OD (a.u.)
Bone
Tooth
CFA
CHA 2
CHA 1
344 346 348 350 352 354 356
Energy (eV)

Figure 6

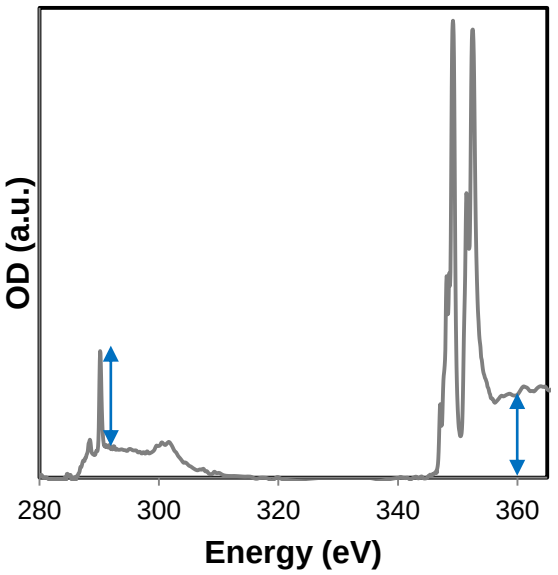

Figure 7

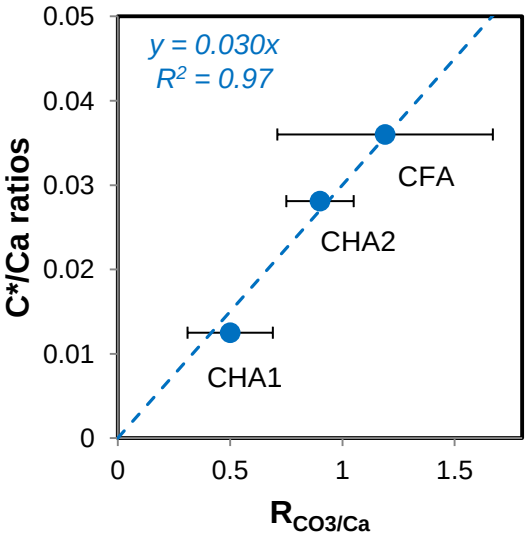
y = 0.030x
R2 = 0.97
CFA
CHA2
CHA1
C*/Ca ratios
RCO3/Ca
0.05
0.04
0.03
0.02
0.01
0
0
0.5
1
1.5

Figure 8

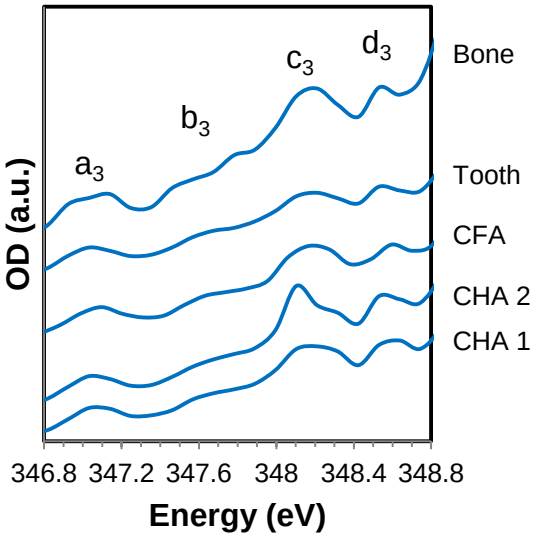
a3
b3
c3
d3
Bone
Tooth
CFA
CHA 2
CHA 1
OD (a.u.)
346.8
347.2
347.6
348
348.4
348.8
Energy (eV)

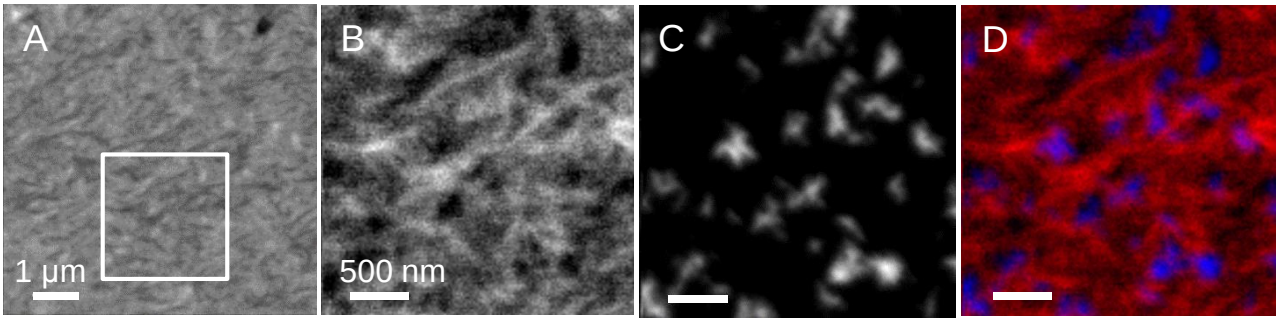
A
1 µm
B
500 nm
C
D

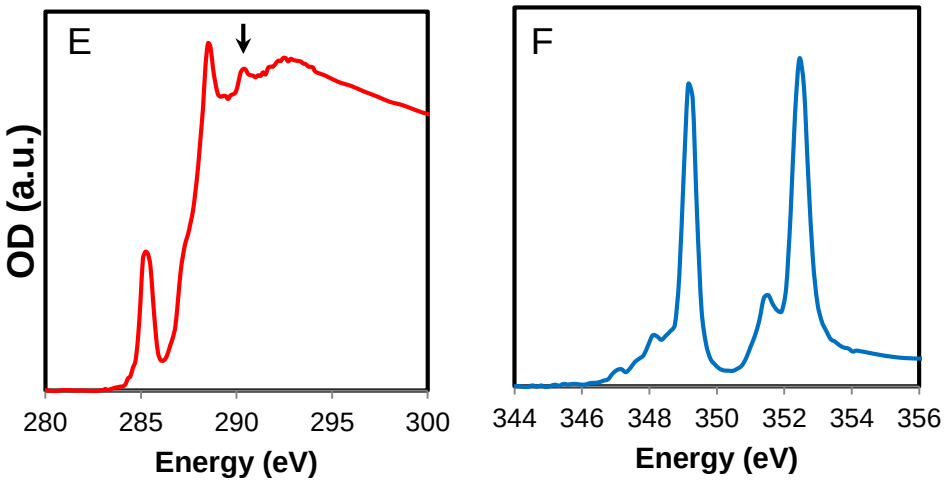
E
OD (a.u.)
280
285
290
295
300
Energy (eV)
F
344
346
348
350
352
354
356
Energy (eV)

*Graphical Abstract

Ca-phosphate biological materials

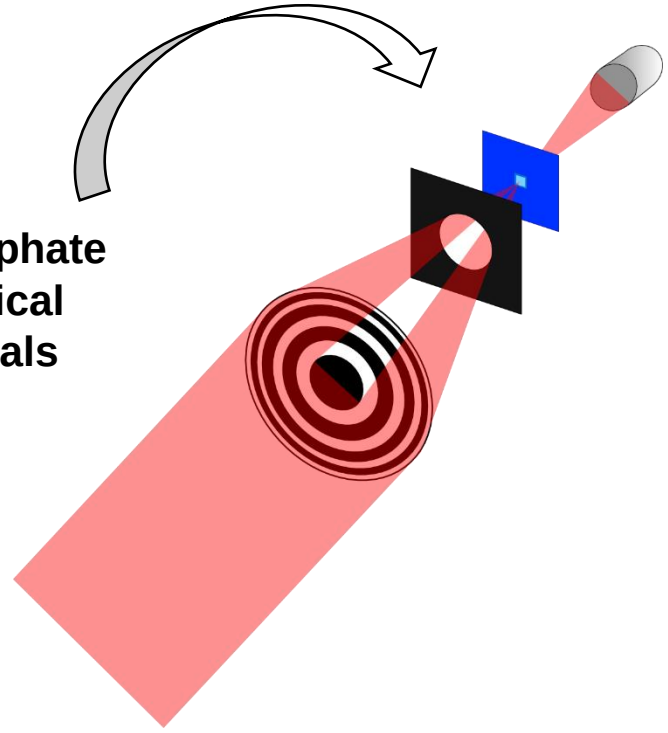

Scanning Transmission X-ray Microscopy

Chemical mapping (~25 nm spatial resolution)

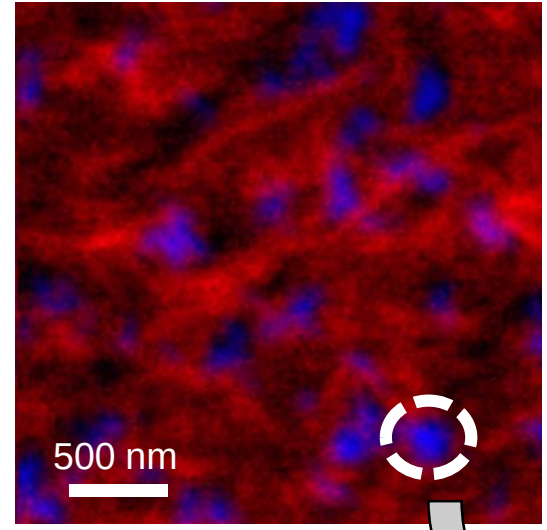

Ca
Corg

XANES spectroscopy